https://doi.org/10.5194/egusphere-2026-1453
Preprint. Discussion started: 25 March 2026

Observation modes of EarthCARE/CPR with different Doppler measurement accuracy: Evaluation of their applicability

Yuki Imura[1], Shunsuke Aoki[1], Takuji Kubota[1], Hirotaka Nakatsuka[1], Yuichi Ohno[1], and Hajime Okamoto[2]

[1]Japan Aerospace Exploration Agency, Tsukuba, Ibaraki 305-8505, Japan
[2]Research Institute for Applied Mechanics, Kyushu University, Fukuoka, Japan

Correspondence to: Yuki Imura (imura.yuki@jaxa.jp)

Abstract. An accurate characterization of cloud vertical motion is essential for understanding cloud microphysical and dynamical processes. The Cloud Profiling Radar (CPR) onboard the Earth Cloud Aerosol and Radiation Explorer (EarthCARE) satellite, launched in May 2024, enables the first global measurements of Doppler velocity from space. The CPR operates in three observation modes—16-km, 18-km, and 20-km modes—each characterized by a distinct pulse repetition frequency (PRF), which determines the Doppler velocity data quality, the maximum observable altitude, and the likelihood of spurious high-altitude echoes known as mirror images. This study quantitatively evaluates the applicability of these three modes using actual CPR observations, focusing on these three aspects. The standard deviation (STD) of Doppler velocity, used as an indicator of measurement noise, indicated that the 16-km and 18-km modes provide more accurate Doppler measurements than the 20-km mode, with comparable STD values between the former two. Clouds above 16 km were primarily observed between 0° and 40° latitude, while clouds exceeding 18 km were rare, suggesting that the 18-km or 20-km modes are suitable for observation in these regions. The risk of overlap between genuine cloud echoes and mirror images at high altitudes was highest in the 16-km and 18-km modes but was largely confined to low-latitude regions (approximately 0°–40°). Accordingly, without considering mirror image-related risks, the 16-km mode is preferable at latitudes above 40°, where high clouds are infrequent and Doppler measurement accuracy is highest. In contrast, the 18-km mode provides an optimal balance between Doppler accuracy and vertical coverage at lower latitudes. It should be noted, however, that high-PRF modes inherently increase the likelihood of mirror image contamination. These results demonstrate, for the first time using actual EarthCARE observations, trade-offs among Doppler measurement accuracy, observation height, and spurious echo contamination across CPR operational modes. Future work should involve continuous assessments of the balance between Doppler accuracy and mirror image contamination to determine the optimal implementation of each mode as a function of latitude.

https://doi.org/10.5194/egusphere-2026-1453
Preprint. Discussion started: 25 March 2026

1 Introduction

Cloud and atmospheric vertical motions are closely linked through both microphysical processes and the surrounding dynamical environment. From a microphysical perspective, variations in cloud particle properties, such as size, density, and phase (liquid or ice), lead to differences in terminal fall velocities, which in turn influence cloud optical properties and radiative heating rates (Albrecht, 1989; Mitchell and Heymsfield, 2005). From a dynamical perspective, updrafts enhance condensation and latent heat release, thereby modulating local atmospheric stability and subsequent cloud development (Betts, 1986; Houze, 1993; Tao et al., 2022). Information on vertical motions is also essential for accurately simulating cloud processes in weather and climate models, because many numerical models have traditionally treated hydrometeor fall velocity as a tuning parameter, which can substantially influence atmospheric circulation and cloud processes (Hourdin et al., 2017; Couvreux et al., 2021). Cloud Doppler velocity, which represents the sum of the reflectivity weighted terminal fall velocity of cloud particles and ambient vertical air motion, is therefore one of the key parameters governing cloud development processes (Radenz et al., 2018; von Terzi et al., 2022). Traditionally, Doppler velocity has been measured using ground-based, ship-based and airborne vertical pointing radars to investigate cloud microphysical properties (e.g., Okamoto et al., 2003; Shupe et al., 2008; Sato et al., 2010; Protat and Williams, 2011; Lamer et al., 2014; Ewald et al., 2019). Doppler fall speed velocity with radar reflectivity measurements turns out to be effective to derive cloud microphysics (Heymsfield et al., 2008; Sato et al., 2009). However, these observations are spatially and temporally limited, making it difficult to statistically characterize vertical cloud processes across diverse regions over long periods of time. To capture global cloud vertical motion and investigate associated aerosol–cloud–radiation interactions, the Earth Cloud Aerosol and Radiation Explorer (EarthCARE; Illingworth et al., 2015; Wehr et al., 2023) satellite was launched in May 2024. EarthCARE carries four state-of-the-art instruments: the Cloud Profiling Radar (CPR), the Atmospheric Lidar (ATLID), the Multi-Spectral Imager (MSI), and the Broad-Band Radiometer (BBR). The CPR, developed by the Japan Aerospace Exploration Agency (JAXA) and the National Institute of Information and Communications Technology (NICT), enables the world's first spaceborne measurements of Doppler velocity from space. This capability provides spatially and temporally uniform data on the vertical structure of clouds, offering valuable insights into the global characteristics of cloud vertical motion.

The CPR onboard EarthCARE measures Doppler velocity using a pulse-pair processing technique, in which Doppler velocities are derived from the coherent detection of phase shifts between successive transmitted pulses. When the CPR observes from a fast-moving satellite platform, the correlation between successive pulses is reduced, leading to increased random noise in the Doppler measurements (referred to as Doppler broadening: Kollias et al., 2023; Hagihara et al., 2023). To mitigate this effect, a higher pulse repetition frequency (PRF) is required, allowing a larger number of pulse samples are acquired within the medium's decorrelation time, thereby reducing random noise and improving Doppler velocity accuracy (Doviak and Zrnic, 1993; Ruzanski et al., 2008; Kollias et al., 2014). A higher PRF also increases the Nyquist velocity, thereby reducing the likelihood of velocity folding. These advantages associated with higher PRF provide the fundamental motivation for employing high-PRF observation modes in the CPR.

https://doi.org/10.5194/egusphere-2026-1453
Preprint. Discussion started: 25 March 2026

However, increasing the PRF imposes limitations on the CPR's maximum unambiguous range. The unambiguous range r_u, defined as $c/(2 \times \mathrm{PRF})$ (where c is the speed of light), becomes shorter as PRF increases, which in turn restricts the observation window and increases susceptibility to second-trip echoes (a phenomenon known as the "Doppler dilemma"; Doviak and Zrnic, 1993). When a transmitted pulse reflects off the ground and, on its return path to the CPR antenna, encounters a cloud that scatters it back toward the surface, the return signal is delayed. As a result, this second-trip echo appears as a false high-altitude feature, referred to as a mirror image (Meneghini and Atlas, 1986; Li and Nakamura, 2002). Similarly, in optically thick clouds such as tropical convective systems, multiple scattering (MS) can generate spurious high-altitude echoes, commonly referred to as MS tails (Battaglia and Simmer, 2008; Battaglia et al., 2010, 2011, 2014, 2016, 2021). These spurious echoes tend to appear more frequently in high-PRF modes owing to the shorter unambiguous range.

This trade-off between Doppler accuracy and unambiguous range motivated the implementation of three CPR observation modes: 16-km, 18-km, and 20-km modes (Imura et al., 2025a, 2025b). These modes are characterized by different PRFs and corresponding maximum observation height. The relationships between latitude, EarthCARE orbit altitude, and PRF are illustrated in Fig. 1. The 16-km mode, which employs the highest PRF range of 7150–7500 Hz, provides the most accurate Doppler velocity measurements. However, its maximum observation height of 16 km is insufficient to fully capture very high-level clouds, such as cirrus or tropical deep convective clouds that extend above this altitude. The 18-km mode, with PRF values ranging from 6800 to 7150 Hz, also achieves relatively high Doppler accuracy, comparable to that of the 16-km mode (as indicated by the green line in Fig. 1), extending the observation range up to 18 km. In contrast, the 20-km mode employs the lowest PRF (6100–6800 Hz), which results in lower Doppler measurement accuracy but allows coverage of very high-level clouds beyond the reach of the 16-km and 18-km modes.

To illustrate the trade-off between Doppler velocity measurement accuracy and observation height, Fig. 2 presents two case studies based on actual CPR observations. Figure 2a shows a time–height cross-section of Doppler velocity observed on 7 November 2024, when CPR operated in the 16-km mode. Figure 2b corresponds to 1 November 2024, during which the CPR operated in the MIX-mode (a combination of the 20-km and 16-km modes). In Fig. 2a, cloud tops extending above 16 km are truncated due to the altitude limit of the 16-km mode, indicating that this mode is insufficient for capturing the full vertical extent of some high clouds. In contrast, regarding Doppler velocity measurement accuracy, the 16-km mode offers a notable advantage: Fig. 2b demonstrates that it yields a smoother Doppler velocity field than the 20-km mode. This suggests that the 16-km mode is subject to lower noise contamination, likely due to its higher PRF. Consequently, the 16-km mode can provide high-quality Doppler velocity measurements at the expense of reduced vertical coverage, whereas the 20-km mode offers greater observation height at the cost of increased measurement noise.

Therefore, when implementing high-PRF modes such as the 16-km and 18-km modes, it is essential to quantitatively assess the trade-off between the advantages of enhanced Doppler measurement accuracy and the disadvantages associated with reduced maximum observation height and increased contamination from spurious echoes. To evaluate the benefits of enhanced Doppler accuracy, previous studies have examined the standard deviation of Doppler velocity as a reliable indicator of Doppler noise levels (Kollias et al., 2014; Burns et al., 2016; Hagihara et al., 2022, 2023). However, these studies relied primarily on

https://doi.org/10.5194/egusphere-2026-1453
Preprint. Discussion started: 25 March 2026

simulated data, and only a limited number have analyzed actual measurements from the EarthCARE/CPR. In this study, we quantified the standard deviation of Doppler velocity derived from different PRF observation modes using actual CPR observations. Furthermore, to assess the drawbacks associated with limited observation height and the occurrence of spurious cloud echoes, we analyzed the global distributions of cloud fraction and the occurrence of mirror images and MS tails. Through these quantitative evaluations, this study discussed the optimal PRF mode configuration for different latitude bands, an issue that remains under active discussion.

The remainder of this paper is organized as follows. Section 2 describes the data and the methods used in this study. Section 3 presents the trade-off analysis among Doppler measurement accuracy, maximum observation height, and spurious cloud echoes. Section 4 summarizes the main conclusions and discusses the applicability of each CPR operational mode across different latitude bands.

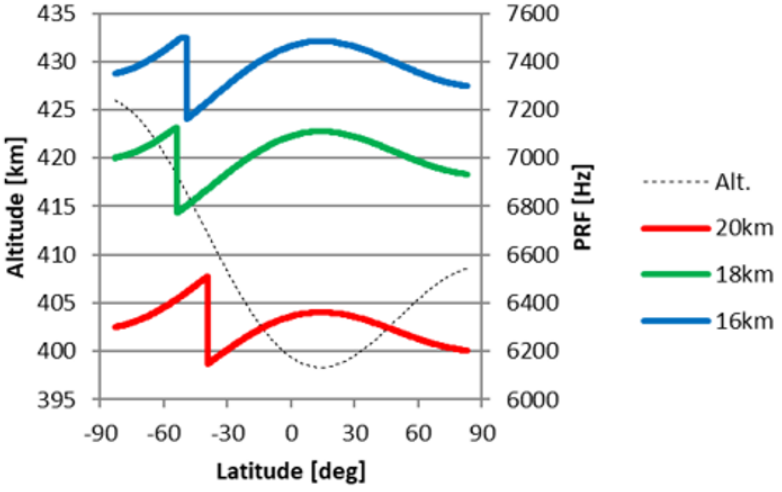

Figure 1: PRF values for each EarthCARE/CPR observation mode as a function of latitude. The 16-km, 18-km, and 20-km modes are shown by blue, green, and red lines, respectively. The black dashed line indicates the EarthCARE orbit altitude.

https://doi.org/10.5194/egusphere-2026-1453
Preprint. Discussion started: 25 March 2026

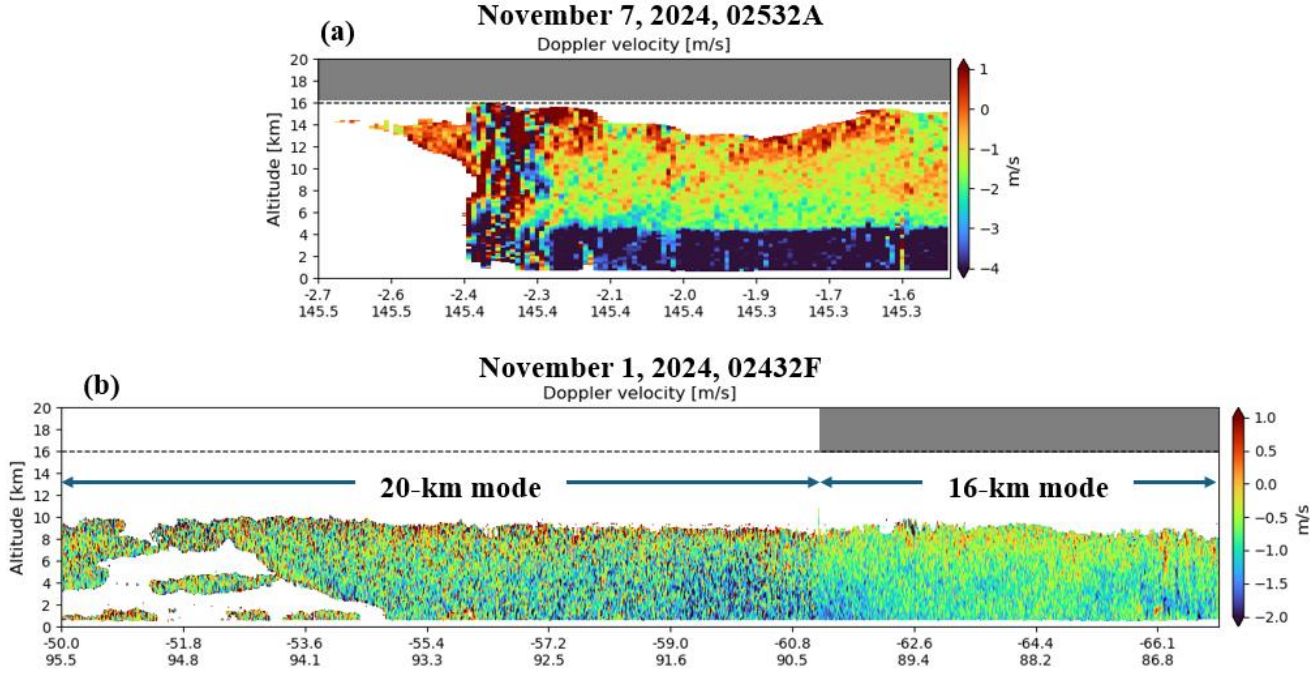

Figure 2: Doppler velocity (m s⁻¹) obtained by EarthCARE/CPR for (a) Frame 02532A acquired on 7 November 2024, and (b) Frame 02432F acquired on 1 November 2024. The upper tick marks on the horizontal axis indicate latitude, while the lower tick marks correspond to longitude. Panel (a) represents a case in which the CPR operated in the 16-km mode, whereas panel (b) shows a case with MIX-mode operation, involving a combination of the 20-km and 16-km modes. In panel (b), cloud regions with reflectivity greater than −20dBZ are displayed, and the regions where the CPR operated in the 20-km and 16-km modes are indicated by two-way arrows. The horizontal dashed lines denote an altitude of 16 km.

2 Data and Methods

2.1 Utilized datasets and methodologies

Science datasets in the EarthCARE mission are summarized in Eisinger et al. (2024). This study employs the CPR L2a one-sensor ECO product, version Ba (JAXA, 2024a), which provides radar reflectivity and Doppler velocity data with horizontal integration lengths of 1-km and 10-km. In JAXA (2024a), Doppler velocity was processed using both bias correction and unfolding correction. The raw Doppler velocity measured by the CPR contains a small bias that exhibits a periodic variation along the satellite's orbit, likely resulting from CPR antenna mispointing or satellite attitude errors (Tanelli et al., 2005; Puigdomènech Treserras et al., 2025). This bias is estimated under the assumption that the horizontally averaged Doppler velocity at the surface bin over a 100-km along track distance should be zero. In addition, the CPR-measured Doppler velocity has uncertainty due to folding or aliasing, and is folded into the range from $-V_{\max}$ to $V_{\max}$, where

$$V_{max} = \frac{\lambda \times PRF}{4}, \quad (1)$$

https://doi.org/10.5194/egusphere-2026-1453
Preprint. Discussion started: 25 March 2026

where λ denotes the CPR pulse wavelength. To mitigate this folding effect, an unfolding correction is applied following the method of Hagihara et al. (2022), which assumes that velocities exceeding 3 m s^{-1} in regions above 0 °C correspond to upward-folded rainfall.

The measured Doppler velocity variance, σ_{vd}^2, includes several uncertainty components and can be expressed as

$$\sigma_{vd}^2 = \sigma_{random}^2 + \sigma_{natural}^2. \quad (2)$$

Here, σ_{random} represents the random noise within the radar beam width and is estimated using the perturbation approximation (Doviak and Zrnic, 1993) as

$$\sigma_{random} = C\sqrt{\frac{\lambda^2}{32\pi^2 M\rho^2\left(\frac{1}{PRF}\right)^2}\left[\left(1+\frac{N}{S}\right)^2 - \rho^2\right]}, \quad (3)$$

where C is a correction factor, M is the number of pulse pairs within the integration length, ρ is the correlation function, and S/N is the signal-to-noise ratio (SNR). The correlation coefficient ρ is given by

$$\rho = \exp\left\{-8\left(\frac{\pi\cdot\sigma_v}{\lambda\cdot PRF}\right)^2\right\}, \quad (4)$$

where σ_v is the total Doppler velocity spectral width. According to Eqs. (3) and (4), higher PRF and SNR reduce random noise, resulting in smaller σ_{vd}^2. Based on these equations, the theoretical relationship between PRF and σ_{random} is calculated, as shown in Fig. 3. In this calculation, the parameter values listed in Table 1 are used. The SNR is set to 2.2 dB at −19 dBZ and is assumed to vary relative to this reference value. When comparing σ_{random} at −19 dBZ using the minimum PRFs of the 20-km, 18-km, and 16-km modes (6100 Hz, 6800 Hz, and 7150 Hz, respectively), the resulting values are 0.60, 0.33, and 0.26 m s^{-1}. These results indicate that the difference in σ_{random} between the 20-km mode and the 18-km and 16-km modes is relatively large, whereas the values for the 18-km and 16-km modes are comparatively similar. This relationship corresponds well to the differences in PRF values shown in Fig. 1. The term $\sigma_{natural}$ represents natural variability, encompassing perturbations in vertical air motion and variations in fall speeds arising from differences in hydrometeor size and density. The standard deviation of Doppler velocity is calculated as described in Section 3.1; however, it should be noted that these values include contributions from both random noise and natural variability.

Parameter	Meaning	Definition	Value	Unit
C	Correction factor	-	1.0	-
λ	Wavelength	$\lambda = c/f$	0.00319	m
f	Frequency	-	94.05	GHz
M	Number of pulse pairs within the integration length	$M = \frac{Li \times PRF \times (NB-1)}{V_s \times 24}$	-	-
Li	Horizontal integration length	-	10	km

https://doi.org/10.5194/egusphere-2026-1453
Preprint. Discussion started: 25 March 2026

NB	Pulse number per a data frame	-	22	-
V_s	Ground track speed of a satellite	-	7,738	m/s
σ_v	Total Doppler velocity spectral width	$\sigma_v^2 = \sigma_{sm}^2 + \sigma_t^2 + \sigma_{psd}^2$	4.01	m/s
σ_{sm}	Spread due to satellite motion	$\sigma_{sm}^2 = (0.3 \times \theta \times V_s)$	3.85	m/s
θ	Antena beam width	$\theta = 0.095 \times \frac{\pi}{180}$	0.00166	rad
σ_t	Spread due to turbulence	Refer to Amayenc et al. (1993)	1.0	m/s
σ_{psd}	Spread due to the distributions of hydrometeor falling velocities	Refer to Gossard et al. (1997)	0.5	m/s

Table 1: Values used for the calculation shown in Fig. 3.

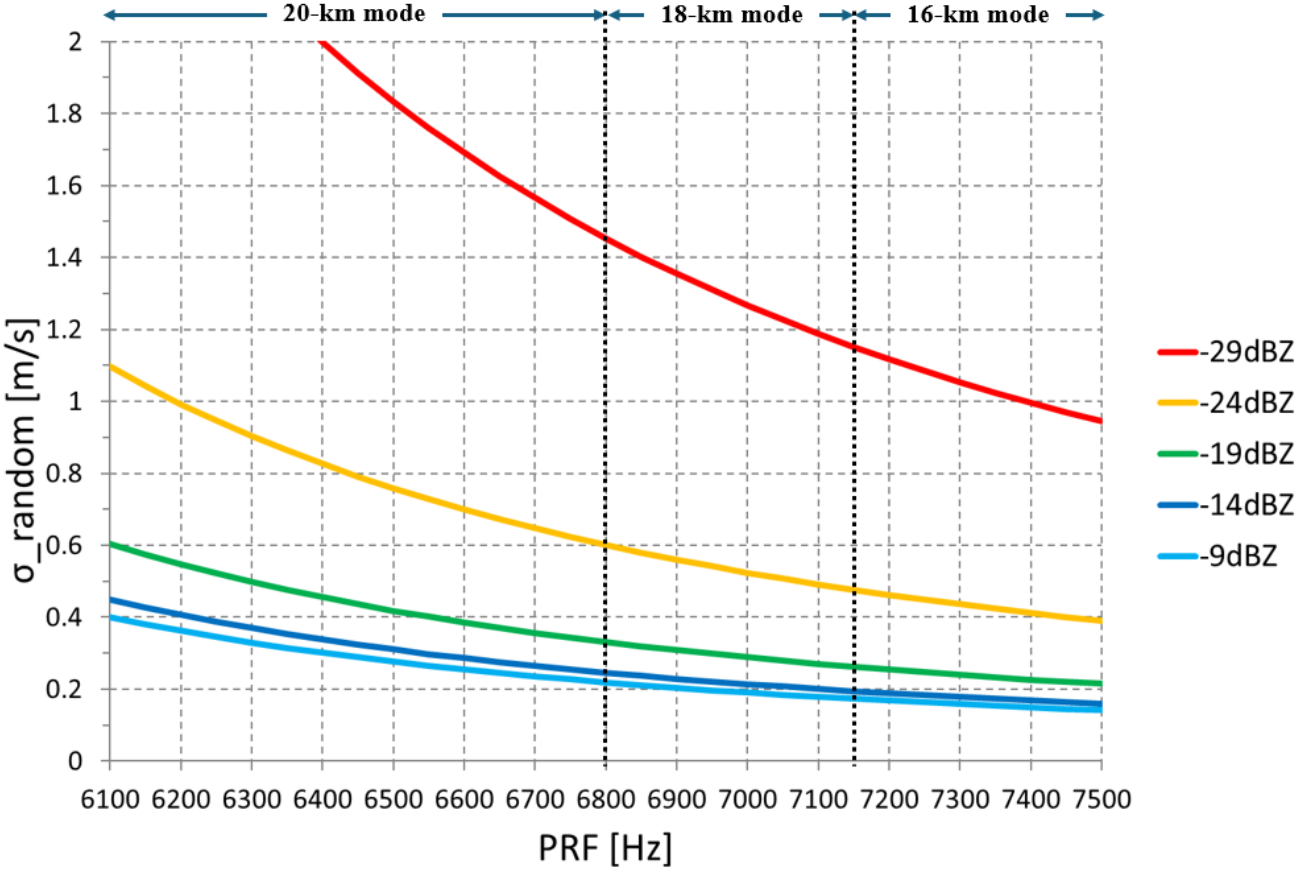

Figure 3: The theoretical relationship between PRF and σ_{random}, calculated using Eqs. (3) and (4) and the parameters listed in Table 1. The PRFs corresponding to the 20-km, 18-km, and 16-km modes are indicated at the top of the figure.

For the identification of cloud areas, the CPR L2a one-sensor CLP product, version Bb (JAXA, 2024b), was utilized (Sato et al., 2025). Cloud areas were defined as regions where the cloud mask value in the product was 30 or higher, and cloud

https://doi.org/10.5194/egusphere-2026-1453
Preprint. Discussion started: 25 March 2026

fraction was defined as the proportion of observations in which clouds were detected relative to the total number of observations. In Section 3.3, the frequency of mirror-echo occurrence was calculated using the mirror echo flag in the CPR L2a ECO product, which identifies second-trip echoes associated with both mirror images and MS tails at two confidence levels, possible and certain. As described in the Algorithm Theoretical Basis Document (ATBD) for the JAXA's Level 2 product (JAXA, 2025), this identification method is based on Battaglia (2021). Here, we used mirror echo flag values greater than zero, i.e., cases in which either mirror images or MS tails were identified with at least possible confidence. Because of uncertainties in estimating mirror-echo reflectivity, a small fraction of mirror echoes and MS signals may remain undetected (Aoki et al., 2025). However, this issue is minor and outside the scope of the present study. Note that second-trip echoes identified by the mirror echo flag in the CPR L2a ECO product have already been removed from the cloud mask in the CPR L2a CLP product.

To further reduce the possibility of such undetected echoes, information from the ATLID sensor was incorporated. ATLID observes the atmosphere simultaneously with the CPR and has higher sensitivity to optically thin clouds. The ATLID L2a one-sensor CLA product, version Ba (JAXA, 2024c), provides a feature mask, which we used to estimate the cloud-top height (Nishizawa et al., 2026). Using this information, CPR-detected clouds were constrained such that their upper boundaries did not exceed the cloud-top height detected by ATLID, thereby more effectively removing mirror image artifacts. This correction is based on the assumption that lidar generally has higher sensitivity to high-level ice cloud particles than cloud radar. It is also noted that joint analysis of cloud top heights from CloudSat and CALIPSO revealed that the global mean fraction of clouds where CloudSat-determined cloud top altitude was higher than that determined by CALIPSO was relatively small (10%) for high-level clouds, though such fractions in low- and mid-level clouds were 26% and 39 %, respectively (Hagihara et al., 2014).

2.2 MIX-mode configuration and special operation of the CPR

In this study, we analyzed CPR observations over a 14-month period from August 2024 to September 2025. During this period, several changes in CPR operating modes occurred, including a major reconfiguration of the MIX-mode in July 2025 and a special observation campaign in November 2024. Because these mode transitions affect the achievable Doppler velocity accuracy, we summarize the relevant operational context here before describing the analysis results in Section 3.

At the beginning of the analysis period, the CPR was operated in the so-called MIX-mode, in which the radar employed the 20-km mode at latitudes below 60° and the 16-km mode at latitudes above 60°. This configuration reflects the fact that deep convective clouds can develop to much higher altitudes in low-latitude regions, while such high clouds are generally absent at high latitudes. The MIX-mode operation continued until 8 July 2025.

On 8 July 2025, the observation mode for latitudes below 60° was switched from the 20-km mode to the 18-km mode to improve Doppler velocity measurement accuracy in low-latitude regions. To evaluate the impact of this change, this study analyzed data from August–September 2024 and August–September 2025 and compared Doppler accuracy before and after the MIX-mode modification (see Section 3.1 for details).

https://doi.org/10.5194/egusphere-2026-1453
Preprint. Discussion started: 25 March 2026

In addition, CPR conducted a special global observation campaign in November 2024. During this period, the CPR operated globally in the 16-km mode from 5 November 2024 21:00:02 to 9 November 2024 00:00:02 UTC, and in the 18-km mode from 9 November 2024 00:00:03 to 12 November 2024 11:50:48 UTC. These operations were preceded by a MIX-mode period, during which the 20-km mode was active at latitudes below 60° from 1 November 2024 00:00:00 to 5 November 2024 21:00:01 UTC. Together, these observations enable a direct comparison of Doppler velocity measurement accuracy among the 16-km, 18-km, and 20-km modes over the same geographic regions and during the same season. Therefore, in our comparative analysis of Doppler accuracy and mirror image characteristics, we focused on latitudes below 60° (see Sections 3.1 and 3.3) and used CPR data from all three operational modes, including the special operation period described above.

2.3 Influence of IQ offset on Doppler velocity measurements

In Doppler radar systems, the IQ offset refers to a direct current (DC) bias added to the in-phase (I) and quadrature (Q) baseband signals due to receiver imperfections, such as mixer imbalance and analog circuit offsets. This offset shifts the I/Q constellation away from the origin and can influence Doppler velocity measurements, particularly in low-reflectivity regions with a low S/N ratio.

CPR is equipped with a nominal and a redundant Signal Processing Unit (SPU-B and SPU-A, respectively), which exhibit different IQ offset characteristics. It is known that the IQ offset of SPU-A, which was refurbished from the engineering model, is larger than that of SPU-B. From the start of observations on 18 June 2024 until 22 June 2024, CPR operated using SPU-B. Due to an operational issue, the active unit was switched from SPU-B to SPU-A on 24 July 2024. The system was then switched back to SPU-B on 26 November 2024, and SPU-B has been in operation since then. The Doppler velocity analysis using data from November 2024, which is the primary focus of this study, corresponds to the period during which CPR was operating with SPU-A. Therefore, to mitigate the impact of IQ offset on Doppler velocity measurements, particularly in noisy low-reflectivity regions, this study focuses on higher-reflectivity regions (greater than –20 dBZ), where radar echoes are more reliable.

3 Result

3.1 Standard deviation of Doppler velocity from CPR

To quantify differences in Doppler velocity data quality among the CPR operational modes, this study calculated the standard deviation (STD) of Doppler velocity, which serves as a useful proxy for sum of Doppler measurement accuracy and natural variabilities of Doppler velocity. This analysis focuses on the latitudinal band from 60°S to 60°N and the period from 1 to 12 November 2024, during which the 16-km and 18-km modes were globally fixed. Figures 4a–4c show the latitude-altitude cross sections of the mean Doppler velocity for each operational mode, while Figs. 4d–4f show the corresponding STDs. We focus on reflectivity between –20 dBZ and 0 dBZ in order to exclude regions with low S/N ratios at very low reflectivity, where the influence of the IQ offset in SPU-A on Doppler velocity measurements is significant, as described in Section 2.3, as well as

https://doi.org/10.5194/egusphere-2026-1453
Preprint. Discussion started: 25 March 2026

regions strongly affected by attenuation at very high reflectivity. Figures 4a–4c indicate that the mean Doppler velocity is generally positive at higher altitudes and negative from the middle to lower troposphere. The large negative Doppler velocities below the 273 K isotherm correspond to rain regions. In Figs. 4d–4f, the large STDs below the 273 K isotherm correspond to rain regions, where a wide range of hydrometeors, from drizzle to raindrops, exhibits a broad spectrum of fall velocities. In contrast, the enhanced STDs near cloud-top altitudes are primarily attributed to the limited number of available cloud samples, as indicated in Figs. 4g–4i. When comparing across operational modes, the 20-km mode exhibits relatively large STDs (Fig. 4f), whereas the 16-km and 18-km modes (Figs. 4d and 4e) show smaller and comparable STD values when STD values are compared at the same latitude and altitude between the two modes. These differences are consistent with the corresponding PRF differences among the modes: the 16-km mode, with the highest PRF, provides more accurate Doppler measurements and thus smaller STDs, while the 20-km mode, with the lowest PRF, exhibits degraded Doppler performance and larger STDs.

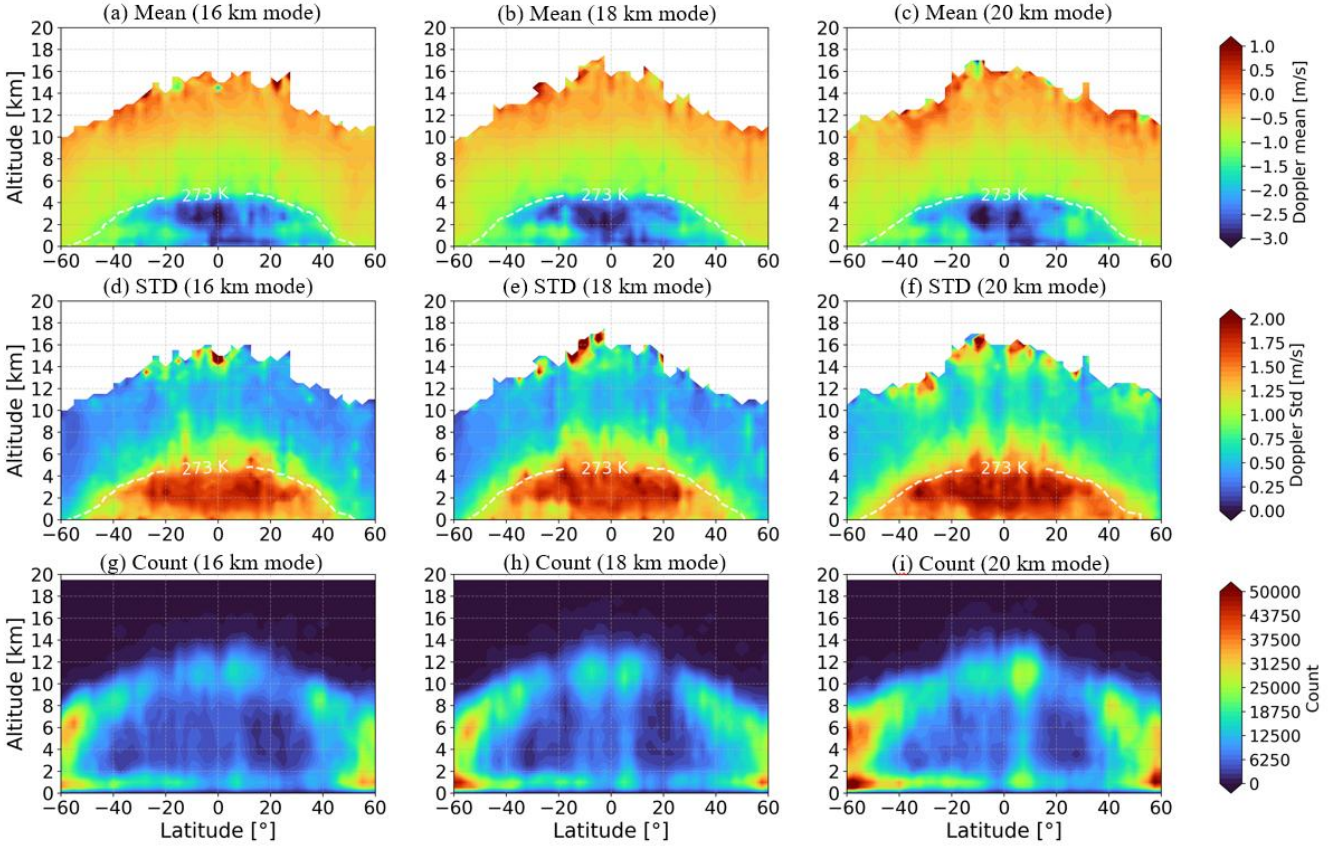

Figure 4: Latitude-altitude cross sections of (a–c) mean Doppler velocity, (d-f) standard deviation of Doppler velocity, and (g–i) cloud sample counts for radar reflectivities between –20 dBZ and 0 dBZ. The 16-km, 18-km, and 20-km modes are shown from left to right. The white dotted line in panels (a–f) indicates the 273.15 K isotherm. Data acquired from 1 to 12 November 2024 were used, and only latitudes within 60°S–60°N are shown. Cloud echoes above the cloud-top heights detected by ATLID were excluded from the analysis.

https://doi.org/10.5194/egusphere-2026-1453
Preprint. Discussion started: 25 March 2026

To further examine how Doppler measurement accuracy depends on the S/N ratio, the dependency of the Doppler velocity STD on radar reflectivity was analyzed. Figures 5a and 5b show the Doppler velocity STDs as a function of radar reflectivity for the 16-km (blue; $STD_{16kmMode}$), 18-km (green; $STD_{18kmMode}$), and 20-km (red; $STD_{20kmMode}$) operational modes. Note that the Doppler STDs include contributions from both random errors and natural variability, as described in Eq. (2). Figures 5c and 5d present the differences in Doppler STDs between the 20-km ($\Delta STD_{20kmMode}$) or 18-km modes ($\Delta STD_{18kmMode}$) and the 16-km mode (in m s^{-1}), defined as

$$\Delta STD_{20kmMode} = \sqrt{STD_{20kmMode}^2 - STD_{16kmMode}^2}, \quad (5)$$

$$\Delta STD_{18kmMode} = \sqrt{STD_{18kmMode}^2 - STD_{16kmMode}^2}. \quad (6)$$

Figure 5e and 5f indicate the relative differences (RDs) in Doppler STDs with respect to the 16-km mode. The RDs for the 20-km mode ($RD_{20kmMode}$) and the 18-km mode ($RD_{18kmMode}$) were calculated as follows:

$$RD_{20kmMode} = \frac{STD_{20kmMode} - STD_{16kmMode}}{STD_{16kmMode}}, \quad (7)$$

$$RD_{18kmMode} = \frac{STD_{18kmMode} - STD_{16kmMode}}{STD_{16kmMode}}. \quad (8)$$

These metrics, defined in Eqs. (5)-(8), quantify the degradation in Doppler observation performance of the 20-km and 18-km modes relative to the 16-km mode, which employs the highest PRF, provided that natural variabilities of clouds/drizzle/precipitation are similar at same radar reflectivity among the three modes and it is expected that these differences between the 20-km or 18-km and the 16-km modes correspond solely to the Doppler velocity measurement accuracy.

Figures 5g and 5h show the corresponding sample counts for each radar reflectivity bin. To ensure consistency across modes, only clouds below 16 km were considered, because clouds detectable by the 18-km and 20-km modes above this altitude are not observable by the 16-km mode. Furthermore, to avoid signal degradation caused by strong attenuation from precipitation, cloud regions below the melting layer were excluded.

The sample counts for each operational mode are comparable in magnitude (on the order of 10^6), thereby ensuring a fair comparison of Doppler velocity STDs. Figures 5a and 5b show a clear decreasing trend in STD with increasing radar reflectivity, which is attributable to improved SNR at higher reflectivity values, as described in Eq. (3). A comparison between integration lengths indicates that the 10-km integration produces smaller STDs than the 1-km integration, reflecting the noise-reduction benefit of temporal and spatial averaging. Across operational modes, the 20-km mode exhibits the largest STDs, whereas the 16-km mode consistently shows the smallest values (see Table 2), indicating that the 16-km mode, which employs the highest PRF, provides the best Doppler measurement performance. The 18-km mode yields STDs comparable to those of the 16-km mode, with only slightly larger values, indicating nearly equivalent Doppler measurement performance. These tendencies are further highlighted in Figs. 5c–5f, which show that the 20-km mode produces substantially larger STD differences (1.25 m s^{-1} and 0.75 m s^{-1} at –20 dBZ for 1-km and 10-km integrations, respectively) and RDs (60% and 56% at –20 dBZ for 1-km and 10-km integrations, respectively), whereas the 18-km mode exhibits much smaller STD differences

https://doi.org/10.5194/egusphere-2026-1453
Preprint. Discussion started: 25 March 2026

(0.53 m s^{-1} and 0.32 m s^{-1} at –20 dBZ for 1-km and 10-km integrations, respectively) and RDs (13% at –20 dBZ for both 1-km and 10-km integrations). These differences tend to decrease with increasing radar reflectivity because of the improvement in S/N; however, the decreasing trend becomes obscure approximately above –15 dBZ. This behavior is consistent with the theoretical results shown in Fig. 3. Overall, these results demonstrate that the 16-km and 18-km modes provide higher Doppler data quality than the 20-km mode and exhibit similar overall Doppler measurement performance. This finding is fully consistent with the theoretical estimates of random Doppler velocity error presented in Fig. 3.

As mentioned earlier, the 18-km mode exhibits substantially better Doppler measurement performance than the 20-km mode; however, the analyses presented in Figs. 4 and 5 were limited to a relatively short period of only a few days. To obtain more statistically robust results and to confirm that the superior Doppler velocity data quality of the 18-km mode, this study extended the analysis period to two months. Specifically, Doppler velocity STDs were analyzed using data from August–September 2024, when the 20-km mode was applied at latitudes within 60°, and from August–September 2025, when the 18-km mode was implemented over the same latitude range. Figure 6 presents the two-month results, including Doppler STDs, STD differences and RDs with respect to the 20-km mode, and sample counts. The number of samples increased substantially compared with Fig. 5 due to the extended analysis period, reaching on the order of 10^7 (Figs. 6g and 6h). Focusing on the Doppler STD, the 18-km mode consistently shows smaller values than the 20-km mode (see Table 3), as illustrated in Figs. 6a and 6b. The STD difference ($\Delta STD^*_{18kmMode}$) and RD ($RD^*_{18kmMode}$) for the 18-km mode (Figs. 6c–6f) were calculated as follows:

$$\Delta STD^*_{18kmMode} = \sqrt{STD^2_{20kmMode} - STD^2_{18kmMode}}, \tag{8}$$

$$RD^*_{18kmMode} = \frac{STD_{20kmMode} - STD_{18kmMode}}{STD_{18kmMode}}. \tag{9}$$

This metric quantifies the improvement in Doppler observation performance of the 18-km mode relative to the 20-km mode, which employs the lowest PRF. Based on the STD differences and RDs, the 18-km mode improves Doppler measurement accuracy by approximately 1.3 m s^{-1} (57%) and 1.0 m s^{-1} (91%) at –20 dBZ for the 1-km and 10-km integrations, respectively. These results of Doppler STDs and RDs provide clear and statistically robust evidence of a substantial enhancement in Doppler measurement accuracy when using a high-PRF mode compared with a low-PRF mode.

https://doi.org/10.5194/egusphere-2026-1453
Preprint. Discussion started: 25 March 2026

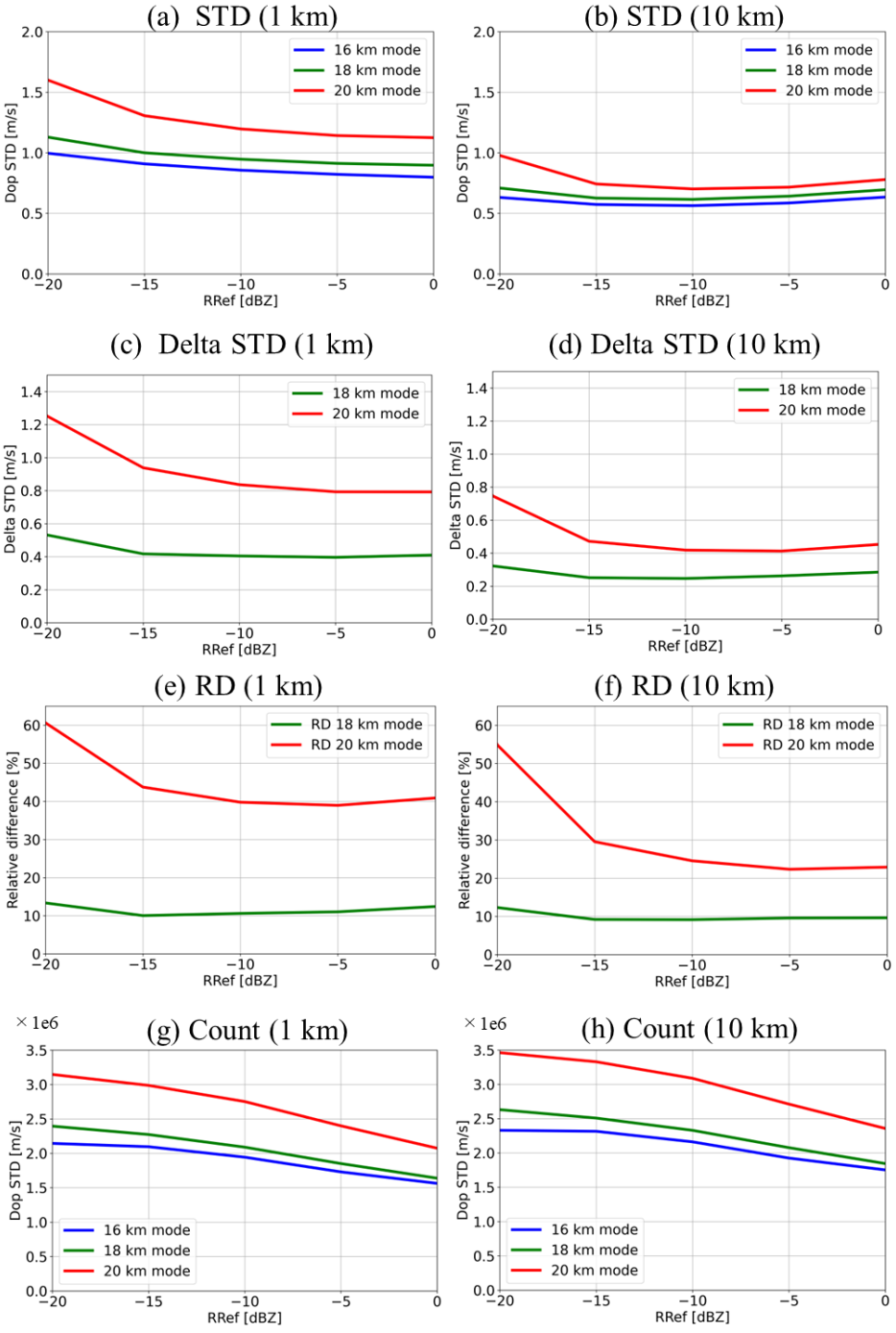

Figure 5: (a, b) STDs of Doppler velocity (m s^{-1}) as a function of radar reflectivity; (c, d) STD differences and (e, f) relative differences (%) of the 18-km and 20-km modes relative to the 16-km mode; and (g, h) sample counts for each radar reflectivity bin. The left and right panels correspond to the 1-km and 10-km integrations, respectively. The 16-km, 18-km, and 20-km modes are indicated by blue, green, and red lines, respectively. Data from 1–12 November 2024 were used, and the analysis region is limited to latitudes within 60°. To ensure a consistent comparison among the modes, only clouds below 16 km were analyzed.

https://doi.org/10.5194/egusphere-2026-1453
Preprint. Discussion started: 25 March 2026

	1-km integration	10-km integration
16-km mode	1.00 m s^{-1}	0.63 m s^{-1}
18-km mode	1.13 m s^{-1}	0.71 m s^{-1}
20-km mode	1.60 m s^{-1}	0.98 m s^{-1}

Table 2: Doppler standard deviation values at –20 dBZ for 1-km and 10-km integrations shown in Figs. 5a and 5b.

https://doi.org/10.5194/egusphere-2026-1453
Preprint. Discussion started: 25 March 2026

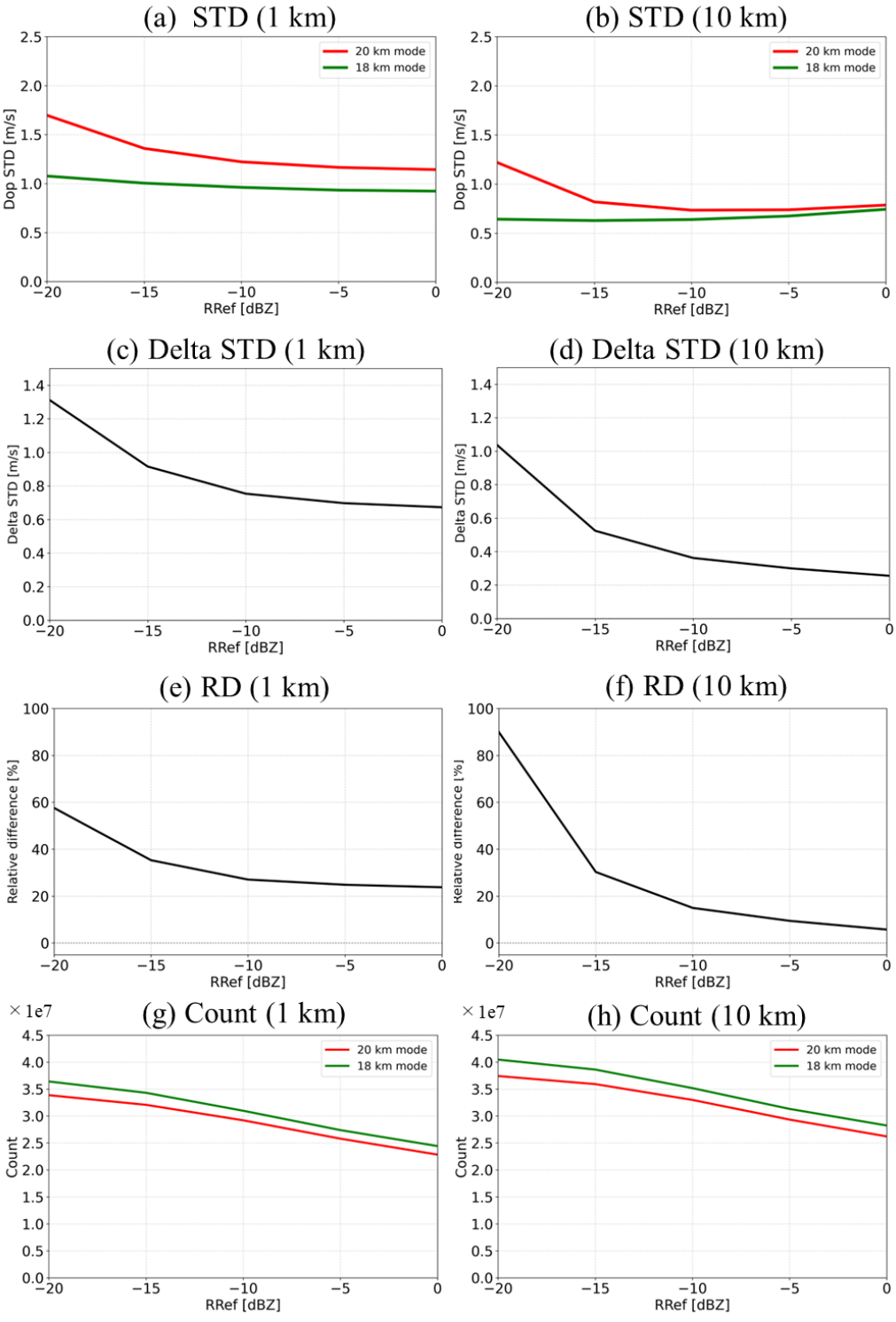

Figure 6: Same as in Fig. 5, but for data periods from August-September 2024 and August-September 2025.

https://doi.org/10.5194/egusphere-2026-1453
Preprint. Discussion started: 25 March 2026

	1-km integration	10-km integration
18-km mode	1.08 m s^{-1}	0.64 m s^{-1}
20-km mode	1.70 m s^{-1}	1.22 m s^{-1}

Table 3: Doppler standard deviation values at –20 dBZ for 1-km and 10-km integrations shown in Figs. 6a and 6b.

3.2 Evaluation of high-level cloud coverage

As mentioned, the high-PRF modes such as the 16-km and 18-km modes offer significant advantages in terms of Doppler measurement accuracy. However, their maximum observation altitudes are lower than that of the 20-km mode, which can detect clouds up to 20 km. This limitation may lead to missed detections of high-level clouds. To assess the feasibility of implementing the 16-km or 18-km modes depending on latitudes, the zonal-mean cloud coverage was examined to identify the latitudinal bands where these operational modes are appropriate.

Figure 7 shows the zonal-mean cloud fractions derived from CPR, averaged over a one-year period from August 2024 to July 2025. The results are displayed on a logarithmic colour scale to emphasize regions of low cloud fraction, and to enhance the visibility of the vertical and latitudinal distributions of cloud occurrence. To avoid contamination by mirror image echoes at high altitudes, as described in Section 2.1, the cloud fractions were corrected such that they do not extend above the cloud-top heights detected by ATLID.

Focusing on the maximum altitude of cloud occurrence, clouds extending above 16 km are roughly primarily observed between latitudes 0° and 40°, suggesting that the 16-km mode can be implemented in the latitude bands of 40°–90°. At lower latitudes, however, high-level convective clouds in the tropics frequently extend above 16 km, rendering the 16-km mode unsuitable in these regions. The globally averaged cloud fractions above 16 km and 18 km are 9.3×10^{-2} and 2.0×10^{-5}, respectively. Given the extremely small cloud fraction above 18 km, the 18-km mode can be applied even in low-latitude regions. Nevertheless, in rare cases, clouds may extend beyond 18 km, such as overshooting tropical convective clouds (Iwasaki et al., 2010 JGR, Bedka et al., 2012; Takahashi and Luo, 2014; Takahashi et al., 2017). Figure 8 provides an example of such an event, showing cloud tops exceeding 18 km as detected by CPR and ATLID. In these instances, the 18-km mode may fail to capture the uppermost portions of the clouds, and this limitation should be considered when applying the mode in low-latitude regions.

https://doi.org/10.5194/egusphere-2026-1453
Preprint. Discussion started: 25 March 2026

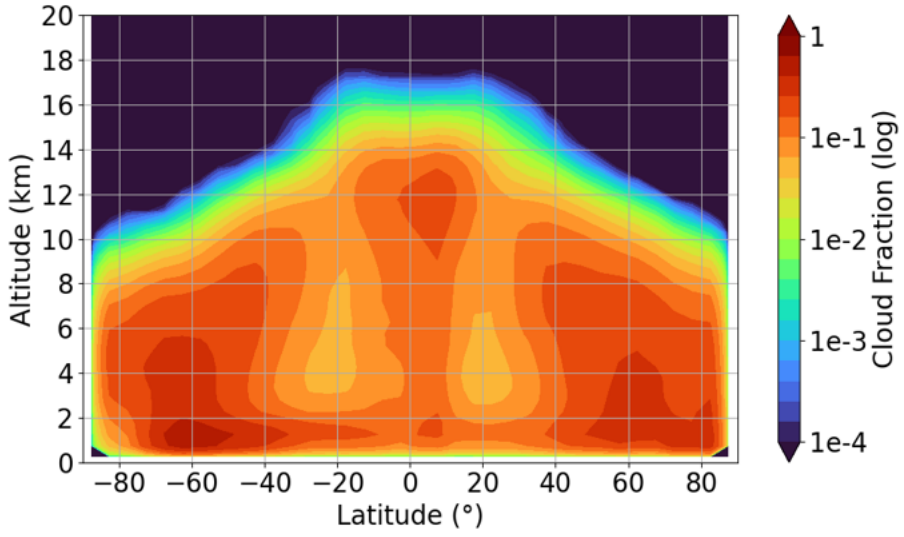

Figure 7: Zonal-mean cloud fraction derived from CPR observations, averaged over a one-year period from August 2024 to July 2025. Values are displayed on a logarithmic scale to highlight regions of low cloud fraction and to emphasize the presence of clouds at high altitudes. Clouds above the cloud-top heights detected by ATLID are excluded from this analysis.

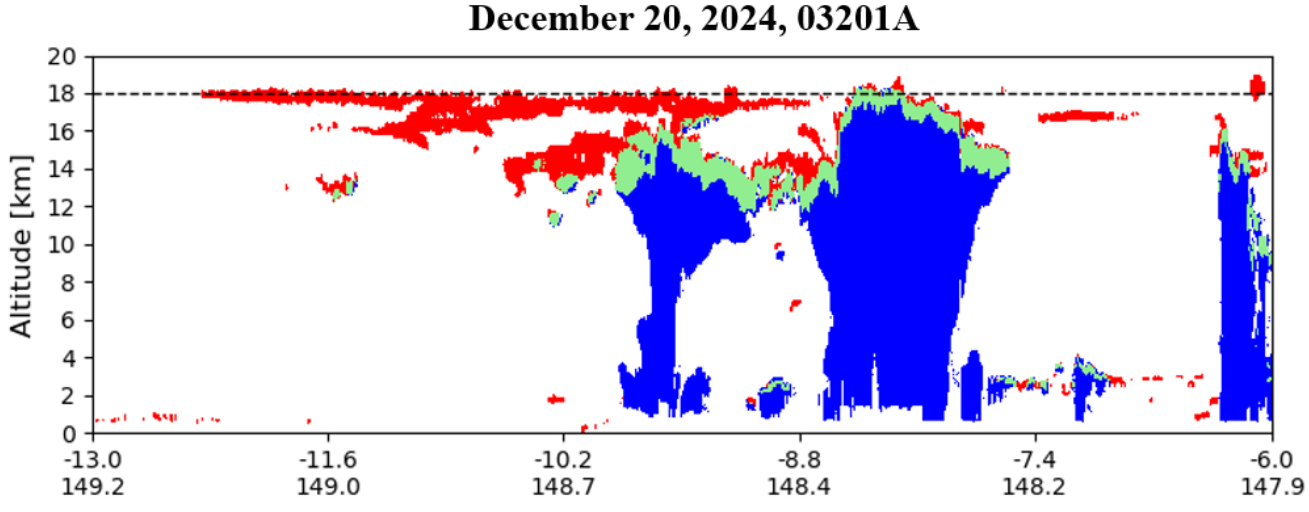

Figure 8: Cloud regions detected by CPR and ATLID for Frame 03201A acquired on December 20, 2024. Red, blue, and green indicate cloud regions detected by ATLID, CPR, and their overlap, respectively. The upper and lower ticks on the horizontal axis denote latitude and longitude, respectively. The dashed line indicates an altitude of 18 km.

3.3 Evaluation of mirror image contamination

In the 16- and 18-km modes, which use higher PRFs, second-trip echoes such as mirror images are more likely to occur, as discussed in Section 3.1. Although the CPR L2a ECO product provides information on the probable locations of mirror images, mirror echo reflectivity values are not provided because of uncertainties in their estimation. As a result, it is difficult to directly

https://doi.org/10.5194/egusphere-2026-1453
Preprint. Discussion started: 25 March 2026

quantify cases in which real clouds overlap with mirror images. Therefore, this study estimates the overlap risk for each operational mode by using the statistical occurrence frequencies of real clouds and mirror images.

Figure 9 shows zonal-mean cloud fraction, mirror image fraction, and the resulting overlap risk between clouds and mirror images for each operational mode, based on data from November 2024. The overlap risk is defined as the product of the cloud fraction and the mirror image fraction, implying that the risk increases when either component is large. The spatial distribution of clouds is generally consistent across the operational modes (Figs. 9a–9c). In contrast, the occurrence characteristics of mirror images differ substantially among the modes: mirror images tend to occur at lower altitudes in the 16-km mode, whereas they appear preferentially at higher altitudes in the 20-km mode (Figs. 9d–9f). Regarding the overlap risk, it is lowest in the 20-km mode, with a global-mean value of 8.0×10^{-5}, and larger in both the 16-km and 18-km modes (2.9×10^{-4} for each; Figs. 9g–9i), corresponding to an increase by a factor of approximately 3.6 relative to the 20-km mode. Focusing on the latitudinal extent of the overlapping regions, these areas extend up to approximately 40° latitude in the 16-km and 18-km modes (Figs. 9g and 9h), whereas they are confined to about 20° latitude in the 20-km mode (Fig. 9i). This result indicates that the 16-km and 18-km modes carry an increased risk of overlap between real cloud echoes and mirror images within roughly 0°–40°, while in the 20-km mode, this potential overlap is largely restricted to approximately 0°–20°.

Figure 10 shows the corresponding vertical profiles of these quantities. Clouds predominantly observed up to approximately 16 km (Fig. 10a), while mirror images begin to occur at altitudes around 10 km in the 16-km and 18-km modes, and around 12 km in the 20-km mode (Fig. 10b). As a result, cloud and mirror image signals overlap primarily between altitudes of roughly 10 and 16 km, as indicated by the overlap risk profile in Fig. 10c. The overlap risk for the 20-km modes peaks at an altitude of approximately 13.75 km, reaching values of 5.3×10^{-5}, whereas the corresponding overlap risks in the 16-km and 18-km modes at the same altitude are 3.3×10^{-4} and 3.6×10^{-4}, respectively, which are approximately 6.3 and 6.8 times larger than that of the 20-km mode. These results indicate that the high-PRF modes carry a substantially higher risk of overlap between real cloud echoes and mirror images. It should also be noted that the mirror echo flag information used in this analysis is incomplete and may occasionally fail to identify mirror images, suggesting that the actual overlap risk may be underestimated in the present results.

https://doi.org/10.5194/egusphere-2026-1453
Preprint. Discussion started: 25 March 2026

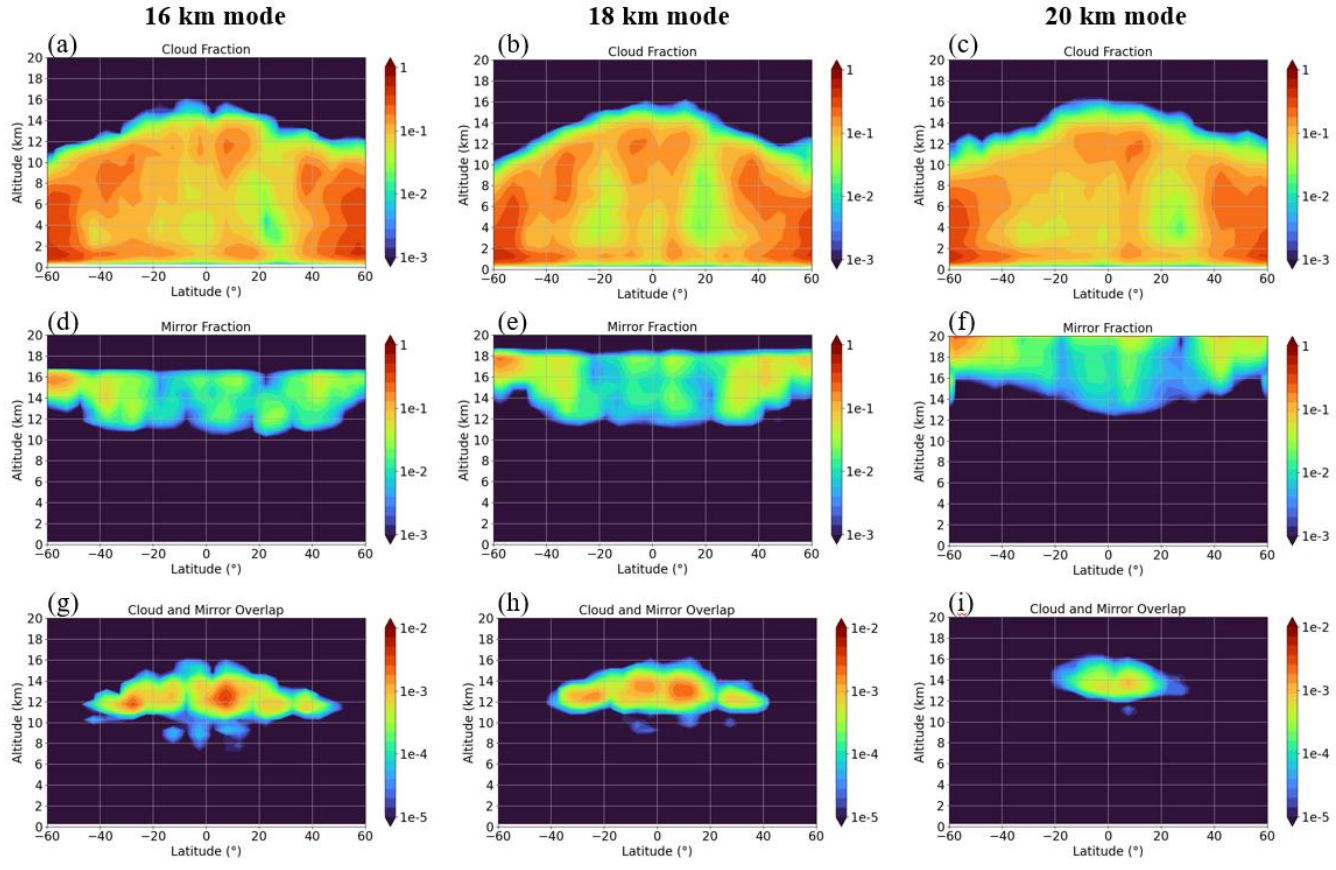

Figure 9: Zonal-mean (a-c) cloud fraction derived from CPR observations, (d-f) mirror image occurrence frequency, and (g-i) overlap risk between cloud and mirror image, defined as the product of the cloud and mirror fractions. Panels (a)-(c) show the mean cloud fractions averaged over the respective observation periods of the 16-km, 18-km, and 20-km modes. Clouds above the cloud-top heights detected by ATLID are excluded in panels (a)-(c). Data from 1–12 November 2024 were used, and the analysis region is limited to latitudes within 60°. All quantities are displayed on a logarithmic scale.

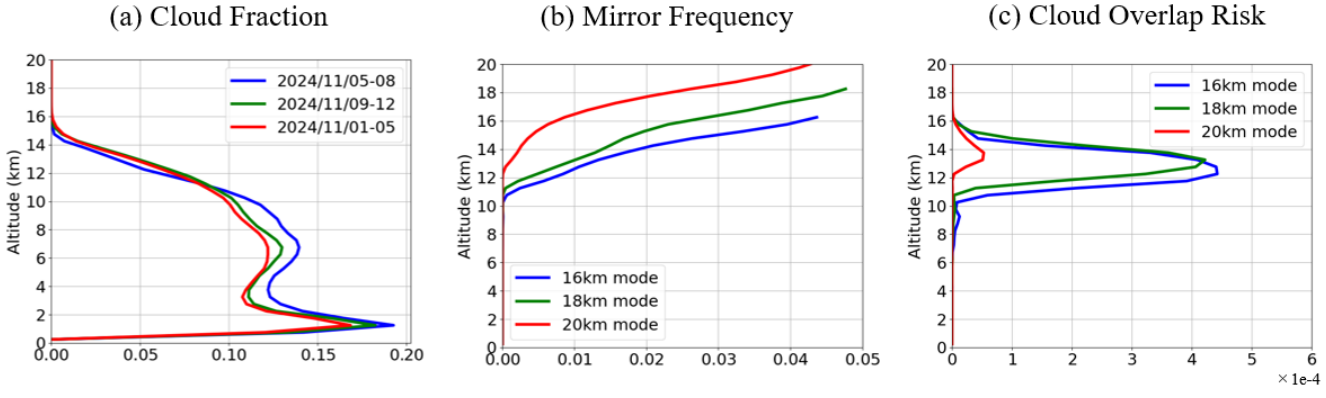

Figure 10: Vertical profiles of (a) cloud fraction, (b) mirror image occurrence frequency, and (c) overlap risk between cloud and mirror image, defined as the product of panels (a) and (b). The 16-km, 18-km, and 20-km modes are indicated by blue, green, and red lines, respectively. In panel (a), the coloured lines represent the mean cloud fractions over the respective observation periods of

https://doi.org/10.5194/egusphere-2026-1453
Preprint. Discussion started: 25 March 2026

each operational modes. Clouds above the cloud-top heights detected by ATLID are excluded in panels (a). The analysis region is limited to latitudes within 60°.

4 Discussion and Conclusion

This study investigated the applicability of the 16-km, 18-km, and 20-km observation modes of the CPR, each characterized by different PRFs and maximum observation altitudes, based on actual CPR observation data, extending earlier simulation-based evaluations. To quantitatively assess and compare the advantages and disadvantages of these three modes, the analysis focused on three key aspects: (1) Doppler velocity measurement accuracy, (2) high-level cloud fraction, and (3) the occurrence frequency of mirror images.

Regarding Doppler measurement accuracy, the STD of Doppler velocity was used as an indicator within the latitudinal range of 60°S–60°N. The largest STD values were found in the 20-km mode, whereas the 16-km and 18-km modes exhibited smaller and comparable STDs (Figs. 4–6). Provided that natural variabilities of cloud contributions in STDs are similar at the same reflectivity among the three modes, the differences in STD between two modes, such as 18-km and 16-km modes, correspond to the differences in Doppler measurement accuracy as a function of radar reflectivity. The relative difference in STD with respect to the 16-km mode was approximately 13% for the 18-km mode, while it was substantially larger (56%) for the 20-km mode at −20 dBZ with a 10-km integration (Fig. 5). These results demonstrate that the 16-km and 18-km modes provide more accurate Doppler velocity measurements than the 20-km mode, with the 18-km mode achieving Doppler accuracy comparable to that of the 16-km mode. Although this performance hierarchy has been theoretically suggested by previous simulation studies, this study confirms it for the first time using actual CPR observation data.

In terms of high-level cloud coverage, clouds exceeding above an altitude of 16 km were primarily observed between approximately 0° and 40° latitude, whereas clouds extended above 18 km were rare within this latitude range (Fig. 7). Accordingly, the 18-km or 20-km mode is appropriate for implementation within the 0°–40° latitude range. In contrast, at higher latitudes, the 16-km mode or 18-km mode is more suitable for ensuring high Doppler measurement accuracy, given the limited occurrence of very high clouds. Regarding mirror image occurrence, the potential overlap between real cloud and mirror image was more frequent in the 16-km and 18-km modes than in the 20-km mode (Figs. 9–10). Such overlap events were largely confined to altitudes between 10 km to 16 km and latitudes between approximately 0° and 40°, indicating that the 16-km and 18-km modes remain applicable at latitudes above 40°, where overlap risk is minimal.

In summary, for latitudes between 0° and 40°, both the 18-km and 20-km modes can be used, as the cloud fraction above 16 km is relatively high, whereas that above 18 km is extremely small in these regions. When the 18-km mode is employed within this latitude band, it provides higher-quality Doppler velocity measurements but entails a greater risk of overlap between real clouds and mirror images compared with the 20-km mode. For latitudes above 40°, all observation modes are suitable in terms of cloud vertical extent; however, the 16-km mode is preferable because it offers the highest Doppler velocity accuracy, cloud occurrence is generally sparse, and the risk of cloud–mirror overlap is low.

https://doi.org/10.5194/egusphere-2026-1453
Preprint. Discussion started: 25 March 2026

Currently, the operational concept of the CPR prioritizes higher Doppler velocity measurement accuracy at the expense of an increased risk of cloud–mirror overlap. Accordingly, the 20-km mode was replaced by the 18-km mode between 0° and 60° during the nominal MIX-mode operation since 8 July 2025. In addition, a further modification to the MIX-mode was implemented on 26 November 2025, whereby the latitude boundary for switching between the 16-km and 18-km modes was shifted from 60° to 40° in order to enhance Doppler data quality in the 40°–60° latitude band. In both cases, the risk of cloud–mirror overlap is expected to increase. In particular, when real cloud echoes and mirror echoes overlap, it is difficult for the mirror echo flag used to identify mirror images to distinguish between them, potentially leading to an underestimation of the overlap risk evaluated in this study. Therefore, continuous and careful quantification of the overlap risk is required in future work. Regarding the evaluation of Doppler measurement accuracy, the Doppler STDs calculated in this study include contributions from natural variability and thus do not represent pure random errors. To better interpret Doppler STDs, future studies should further validate the CPR Doppler measurements using independent observations, such as ground-based or aircraft-borne radars operating in coordination with EarthCARE underflights (e.g., HG-SPIDER; Horie et al., 2000, HALO/HAMP; Mech et al., 2014; Ewald et al., 2019). Furthermore, in the tropics, rare overshooting convective clouds can exceed altitudes of 18 km. In such cases, the 18-km mode cannot fully capture the uppermost portions of these clouds. Thus, a statistical analysis of cloud fractions above 18 km in the tropics, based on ATLID observations, should be conducted in future studies.

Overall, the findings of this study highlight the inherent trade-off between Doppler measurement accuracy and the risk of mirror image occurrence across the three CPR observation modes. Discussions on the optimal implementation of observation modes for each latitude band are currently ongoing.

Author contribution

YI analyzed the satellite data and prepared the initial draft of the manuscript. SA provided the dataset necessary for evaluating the mirror image. TK advised on the study direction and provided helpful comments. HN, YO, and HO provided technical suggestions, interpretation of physical meaning and valuable feedback for the analysis.

Competing interests

At least one of the co-authors serves as editor for the special issue to which this paper belongs.

Acknowledgments.

The authors would like to thank the scientists at ESA-JAXA EarthCARE Joint Mission Advisory Group (JMAG) and Quality Working Group (QWG) for their helpful comments and advice. In particular, the authors greatly appreciate Hiroaki Horie for providing insightful comments on the analyses. Hajime Okamoto is supported in part by the Japan Aerospace

https://doi.org/10.5194/egusphere-2026-1453
Preprint. Discussion started: 25 March 2026

Exploration Agency for the EarthCARE Mission (EORA3 and EORA4), in part by JSPS KAKENHI Grant number JP24H00275 and by the Collaborative Research Program of the Research Institute for Applied Mechanics, Kyushu University.
This paper was edited for English language quality using an AI-based tool.

References

Albrecht, B. A., 1989: Aerosols, cloud microphysics, and fractional cloudiness. Science, 245, 1227–1230, https://doi.org/10.1126/science.245.4923.1227.

Amayenc, P., Testud, J., and Marzoug, M.: Proposal for a Spaceborne Dual-Beam Rain Radar with Doppler Capability, J. Atmos. Ocean. Technol., 10, 262–276, https://doi.org/10.1175/1520-0426(1993)010<0262:PFASDB>2.0.CO;2, 1993.

Aoki, S., Kubota, T., and Horie, H.: Second-trip echoes appeared in EarthCARE/CPR: Characteristics and mitigation performances in JAXA CPR L2a Product, 2nd ESA-JAXA EarthCARE In-Orbit Validation Workshop Frascati, Italy, 17–20 March 2025, https://airdrive.eventsair.com/eventsairwesteuprod/production-nikal-public/2d6d6bd6fc524b5082cf2c8b0855c7bc (last access: 6 January 2026), 2025.

Battaglia, A.: Impact of second-trip echoes for space-borne high-pulse-repetition-frequency nadir-looking W-band cloud radars, Atmos. Meas. Tech., 14, 7809–7820, https://doi.org/10.5194/amt-14-7809-2021, 2021.

Battaglia, A. and Simmer, C.: How Does Multiple Scattering Affect the Spaceborne W-Band Radar Measurements at Ranges Close to and Crossing the Sea-Surface Range?, IEEE T. Geosci. Remote, 46, 1644–1651, https://doi.org/10.1109/TGRS.2008.916085, 2008.

Battaglia, A., Tanelli, S., Kobayashi, S., Zrnic, D., Hogan, R. J., and Simmer, C.: Multiple-scattering in radar systems: A review, J. Quant. Spectrosc. Ra., 111, 917–947, https://doi.org/10.1016/j.jqsrt.2009.11.024, 2010.

Battaglia, A., Augustynek, T., Tanelli, S., and Kollias, P.: Multiple scattering identification in spaceborne W-band radar measurements of deep convective cores, J. Geophys. Res., 116, D19201, https://doi.org/10.1029/2011JD016142, 2011.

Battaglia, A., Tanelli, S., Heymsfield, G. M., and Tian, L.: The Dual Wavelength Ratio Knee: A Signature of Multiple Scattering in Airborne Ku–Ka Observations, J. Appl. Meteorol. Clim., 53, 1790–1808, https://doi.org/10.1175/JAMC-D-13-0341.1, 2014.

https://doi.org/10.5194/egusphere-2026-1453
Preprint. Discussion started: 25 March 2026

Battaglia, A., Mroz, K., Tanelli, S., Tridon, F., and Kirstetter, P.-E.: Multiple-Scattering-Induced "Ghost Echoes" in GPM DPR Observations of a Tornadic Supercell, J. Appl. Meteorol. Clim., 55, 1653–1666, https://doi.org/10.1175/JAMC-D-15-0136.1, 2016.

Bedka, K. M., Dworak, R., Brunner, J., and Feltz, W.: Validation of Satellite-Based Objective Overshooting Cloud-Top Detection Methods Using *CloudSat* Cloud Profiling Radar Observations, Journal of Applied Meteorology and Climatology, 51(10), 1811-1822, https://doi.org/10.1175/JAMC-D-11-0131.1, 2012.

Betts, A. K., and Miller, M. J.: A new convective adjustment scheme. Part 11: Single column tests using GATE wave, BOMEX, ATEX and arctic air-mass data sets, Quart. J. R. Met. SOC, 112, 693–709, https://doi.org/10.1002/qj.49711247308, 1986.

Burns, D., P. Kollias, A. Tatarevic,A. Battaglia, and S. Tanelli, The performance of the EarthCARE Cloud Profiling Radar in marine stratiform clouds, J. Geophys. Res. Atmos., 121, 14, 525–14, 537, https://doi.org/10.1002/2016JD025090, 2016.

Couvreux, F., Hourdin, F., Williamson, D., Roehrig, R., Volodina, V., Villefranque, N., et al.: Process-based climate model development harnessing machine learning: I. Acalibration tool for parameterization improvement. Journal of Advances in Modeling Earth Systems, 13, e2020MS002217, https://doi.org/10.1029/2020MS002217, 2021.

Doviak, R. J. and Zrnic, D. S.: Doppler Radar and Weather Observations, Academic Press, San Diego, CA, 2nd edn., 592 pp., ISBN 978-0-12-221422-6, 1993.

Eisinger, M., Marnas, F., Wallace, K., Kubota, T., Tomiyama, N., Ohno, Y., Tanaka, T., Tomita, E., Wehr, T., and Bernaerts, D.: The EarthCARE mission: science data processing chain overview, Atmos. Meas. Tech., 17, 839–862, https://doi.org/10.5194/amt-17-839-2024, 2024.

Ewald, F., Groß, S., Hagen, M., Hirsch, L., Delanoë, J., and Bauer-Pfundstein, M.: Calibration of a 35 GHz airborne cloud radar: lessons learned and intercomparisons with 94 GHz cloud radars, Atmos. Meas. Tech., 12, 1815–1839, https://doi.org/10.5194/amt-12-1815-2019, 2019.

Gossard, E. E., Snider, J. B., Clothiaux, E. E., Martner, B., Gibson, J. S., Kropfli, R. A., and Frisch, A. S.: The potential of 8-mm radars for remotely sensing cloud drop size distributions, J. Atmos. Ocean. Technol., 14, 76–87, https://doi.org/10.1175/1520-0426(1997)014<0076:TPOMRF>2.0.CO;2, 1997.

https://doi.org/10.5194/egusphere-2026-1453
Preprint. Discussion started: 25 March 2026

Hagihara, Y., Okamoto, H., and Luo Z. J.: Joint analysis of cloud top heights from CloudSat and CALIPSO: New insights into cloud top microphysics, J. Geophys. Res. Atmos., 119, 4087–4106, https://doi.org/10.1002/2013JD020919, 2014.

Hagihara, Y., Ohno, Y., Horie, H., Roh, W., Satoh, M., Kubota, T., and Oki, R.: Assessments of Doppler velocity errors of EarthCARE cloud profiling radar using global cloud system resolving simulations: Effects of Doppler broadening and folding, IEEE Trans. Geosci. Remote Sens., 60, 1–9, https://doi.org/10.1109/TGRS.2021.3060828, 2022.

Hagihara, Y., Ohno, Y., Horie, H., Roh, W., Satoh, M., and Kubota, T.: Global evaluation of Doppler velocity errors of EarthCARE cloud-profiling radar using a global storm-resolving simulation, Atmos. Meas. Tech., 16, 3211–3219, https://doi.org/10.5194/amt-16-3211-2023, 2023.

Horie, H., Iguchi, T., Hanado, H., Kuroiwa, H., Okamoto, H., and Kumagai, H.: Development of a 95-GHz Airborne Cloud Profiling Radar (SPIDER) --Technical Aspects--, IEICE TRANSACTIONS on Communications, E83-B, 2010–2020, 2000.

Hourdin, F., Mauritsen, T., Gettelman, A., Golaz, J., Balaji, V., Duan, Q., Folini, D., Ji, D., Klocke, D., Qian, Y., Rauser, F., Rio C., Tomassini, L., Watanabe, M., and Williamson, D.: The Art and Science of Climate Model Tuning, Bulletin of the American Meteorological Society, 98(3), 589–602, https://doi.org/10.1175/BAMS-D-15-00135.1, 2017.

Houze, R. A.: Cloud Dynamics, Academic Press, San Diego, CA, USA, 573 pp., 1993.

Illingworth, A. J., Barker, H. W., Beljaars, A., Ceccaldi, M., Chepfer, H., Clerbaux, N., Cole, J., Delanoë, J., Domenech, C., Donovan, D. P., Fukuda, S., Hirakata, M., Hogan, R. J., Huenerbein, A., Kollias, P., Kubota, T., Nakajima, T., Nakajima, T. Y., Nishizawa, T., ... Wehr, T.: The EarthCARE satellite: The next step forward in global measurements of clouds, aerosols, precipitation, and radiation, Bulletin of the American Meteorological Society, 96(8), 1311–1332. https://doi.org/10.1175/BAMS-D-12-00227.1, 2015.

Imura, Y., Tomita, E., Nio, T., Okada, K., Maruyama, K., Nakatsuka, H., Tomiyama, N., Aida, Y., Haze, K., Ochiai, S., Konoue, K., Kubota, T., Tanaka, T., Muto, M., Aoki, S., Horie, H., Ohno, Y., and Sato, K.: EarthCARE/CPR current conditions and preliminary results from scientific views, Remote Sensing of the Atmosphere, Clouds, and Precipitation VIII. Vol. 13262. SPIE, https://doi.org/10.1117/12.3045833, 2025a.

Imura, Y., Aoki, S., Kubota, T., and Nakatsuka, H.: Doppler Velocity Measured by the World's First Spaceborne Doppler Radar: Evaluations of Observation Modes in EarthCARE/CPR, IGARSS 2025 - 2025 IEEE International Geoscience and

https://doi.org/10.5194/egusphere-2026-1453
Preprint. Discussion started: 25 March 2026

Remote Sensing Symposium, Brisbane, Australia, pp. 1528-1531, https://doi.org/10.1109/IGARSS55030.2025.11244044, 2025b.

Iwasaki, S., Shibata, T., Nakamoto, J., Okamoto, H., Ishimoto, H., and Kubota, H.: Characteristics of deep convection measured by using the A-train constellation, J. Geophys. Res., 115, D06207, https://doi.org/10.1029/2009JD013000, 2010.

JAXA, EarthCARE/CPR L2a CPR one-sensor Echo Product. https://doi.org/10.57746/EO.01jdvd0xm10ema4rxwbpcd0dn1, 2024a.

JAXA, EarthCARE/CPR L2a CPR one-sensor Cloud Products. https://doi.org/10.57746/EO.01jdvd2gqq34e6yz9p8kfe68x5, 2024b.

JAXA, EarthCARE/ATLID L2a ATLID one-sensor Cloud Aerosol Products. https://doi.org/10.57746/EO.01jkwjk45jrx9frz6c11x4rs8e, 2024c.

JAXA, EarthCARE JAXA Level-2 Algorithm Theoretical Basis Document, available at: https://www.eorc.jaxa.jp/EARTHCARE/document/JAXAL2ProductList/ATBD/EarthCARE_JAXA_L2_ATBD_verN_Dec2025.pdf (last access: 16 March 2026), 2025.

Kollias, P., Tanelli, S., Battaglia, A., and Tatarevic, A.: Evaluation of EarthCARE Cloud Profiling Radar Doppler Velocity Measurements in Particle Sedimentation Regimes, Journal of Atmospheric and Oceanic Technology, 31(2), 366-386, https://doi.org/10.1175/JTECH-D-11-00202.1, 2014.

Kollias, P., Puidgomènech Treserras, B., Battaglia, A., Borque, P. C., and Tatarevic, A.: Processing reflectivity and Doppler velocity from EarthCARE's cloud-profiling radar: the C-FMR, C-CD and C-APC products, Atmos. Meas. Tech., 16, 1901–1914, https://doi.org/10.5194/amt-16-1901-2023, 2023.

Lamer, K., Tatarevic, A., Jo, I., and Kollias, P.: Evaluation of gridded scanning ARM cloud radar reflectivity observations and vertical doppler velocity retrievals, Atmos. Meas. Tech., 7, 1089–1103, https://doi.org/10.5194/amt-7-1089-2014, 2014.

Li, J. and Nakamura, K.: Characteristics of the Mirror Image of Precipitation Observed by the TRMM Precipitation Radar, J. Atmos. Ocean. Tech., 19, 145–158, https://doi.org/10.1175/1520-0426(2002)019, 2002.

https://doi.org/10.5194/egusphere-2026-1453
Preprint. Discussion started: 25 March 2026

Mech, M., Orlandi, E., Crewell, S., Ament, F., Hirsch, L., Hagen, M., Peters, G., and Stevens, B.: HAMP – the microwave package on the High Altitude and LOng range research aircraft (HALO), Atmos. Meas. Tech., 7, 4539–4553, https://doi.org/10.5194/amt-7-4539-2014, 2014.

Meneghini, R. and Atlas, D.: Simultaneous Ocean Cross Section and Rainfall Measurements from Space with a Nadir-Looking Radar, J. Atmos. Ocean. Tech., 3, 400–413, https://doi.org/10.1175/1520-0426(1986)003<0400:SOCSAR>2.0.CO;2, 1986.

Mitchell, D. L. and Heymsfield A. J.: Refinements in the Treatment of Ice Particle Terminal Velocities, Highlighting Aggregates, Journal of the Atmospheric Sciences, 1637–1644, 62(5), https://doi.org/10.1175/JAS3413.1, 2005.

Okamoto, H., Iwasaki, S., Yasui, M., Horie, H., Kuroiwa, H., and Kumagai, H.: An algorithm for retrieval of cloud microphysics using 95-GHz cloud radar and lidar, J. Geophys. Res., 108(D7), 4226, https://doi.org/10.1029/2001JD001225, 2003.

Okamoto, H., Sato, K., Nishizawa, T., Jin, Y., Ogawa, S., Ishimoto, H., Hagihara, Y., Oikawa, E., Kikuchi, M., Satoh, M., and Roh, W.: Cloud masks and cloud type classification using EarthCARE CPR and ATLID, Atmos. Meas. Tech. Discuss. [preprint], https://doi.org/10.5194/amt-2024-103, 2024.

Protat, A. and Williams R. C.: The Accuracy of Radar Estimates of Ice Terminal Fall Speed from Vertically Pointing Doppler Radar Measurements, Journal of Applied Meteorology and Climatology, 50(10), 2120–2138, https://doi.org/10.1175/JAMC-D-10-05031.1, 2011.

Puigdomènech Treserras, B., Kollias, P., Battaglia, A., Tanelli, S., and Nakatsuka, H.: EarthCARE's cloud profiling radar antenna pointing correction using surface Doppler measurements, Atmos. Meas. Tech., 18, 5607–5618, https://doi.org/10.5194/amt-18-5607-2025, 2025.

Radenz, M., Bühl, J., Lehmann, V., Görsdorf, U., and Leinweber, R.: Combining cloud radar and radar wind profiler for a value added estimate of vertical air motion and particle terminal velocity within clouds, Atmos. Meas. Tech., 11, 5925–5940, https://doi.org/10.5194/amt-11-5925-2018, 2018.

Ruzanski, E., Hubbert, C. J., and Chandrasekar, V.: Evaluation of the Simultaneous Multiple Pulse Repetition Frequency Algorithm for Weather Radar, Journal of Atmospheric and Oceanic Technology, 25(7), 1166-1181, https://doi.org/10.1175/2007JTECHA1042.1, 2008.

https://doi.org/10.5194/egusphere-2026-1453
Preprint. Discussion started: 25 March 2026

Sato, K., Okamoto, H., Yamamoto, K. M., Fukao, S., Kumagai, H., Ohno, Y., Horie, H., and Abo, M.: 95-GHz Doppler radar and lidar synergy for simultaneous ice microphysics and in-cloud vertical air motion retrieval, J. Geophys. Res., Atmos., 114(D3), D03203-1–D03203-17, https://doi.org/10.1029/2008JD010222, 2009.

Sato, K., Okamoto, H., Takemura, T., Kumagai, H., and Sugimoto, N.: Characterization of ice cloud properties obtained by shipborne radar/lidar over the tropical western Pacific Ocean for evaluation of an atmospheric general circulation model, J. Geophys. Res., 115, D15203, https://doi.org/10.1029/2009JD012944, 2010.

Sato, K., Okamoto, H., Nishizawa, T., Jin, Y., Nakajima, Y. T., Wang, M., Satoh, M., Roh, W., Ishimoto, H., and Kudo, R.: JAXA level 2 cloud and precipitation microphysics retrievals based on EarthCARE radar, Lidar, and imager: The CPR CLP, AC CLP, and ACM CLP products, Atmos. Meas. Techn., 18(5), 1325–1338, 2025.

Shupe, M. D., Kollias, P., Matrosov, S. Y., and Schneider, T. L.: Deriving mixed-phase cloud properties from Doppler radar spectra. Journal of Atmospheric and Oceanic Technology, 25(4), 556–573. https://doi.org/10.1175/2007JTECHA1007.1, 2008

Takahashi, H., and Luo, Z. J.: Characterizing tropical overshooting deep convection from joint analysis of CloudSat and geostationary satellite observations, J. Geophys. Res. Atmos., 119, 112–121, https://doi.org/10.1002/2013JD020972, 2014.

Takahashi, H., Luo Z. J., and Stephens, G. L.: Level of neutral buoyancy, deep convective outflow, and convective core: New perspectives based on 5 years of CloudSat data, J. Geophys. Res. Atmos., 122, 2958–2969, https://doi.org/10.1002/2016JD025969, 2017.

Tanelli, S., Im, E., Kobayashi, S., Mascelloni, R., and Facheris, L.: Spaceborne Doppler radar measurements of rainfall: Correction of errors induced by pointing uncertainties, J. Atmos. Ocean. Technol., 22, 1676–1690, 2005.

Tao, W.-K., Iguchi, T., Lang, S., Li, X., Mohr, K., Matsui, T., van den Heever, S. C., and Braun, S.: Relating Vertical Velocity and Cloud/Precipitation Properties: A Numerical Cloud Ensemble Modeling Study of Tropical Convection, Journal of Advances in Modeling Earth Systems, 14(9), e2021MS002677, https://doi.org/10.1029/2021MS002677, 2022.

von Terzi, L., Dias Neto, J., Ori, D., Myagkov, A., and Kneifel, S.: Ice microphysical processes in the dendritic growth layer: a statistical analysis combining multi-frequency and polarimetric Doppler cloud radar observations, Atmos. Chem. Phys., 22, 11795–11821, https://doi.org/10.5194/acp-22-11795-2022, 2022

Wehr, T., Kubota, T., Tzeremes, G., Wallace, K., Nakatsuka, H., Ohno, Y., and Bernaerts: The EarthCARE mission–science and system overview, Atmos. Meas. Tech., 16, 3581–3608, 2023.